CHEMISTRY OF MATERIALS

ARTICLE

pubs.acs.org/cm

How Nanoparticles Coalesce: An in Situ Study of Au Nanoparticle Aggregation and Grain Growth

Bridget Ingham,[*,†,‡] Teck H. Lim,[§] Christian J. Dotzler,[†,∥] Anna Henning,[§] Michael F. Toney,[∥] and Richard D. Tilley[‡,§]

[†]Industrial Research Limited, P.O. Box 31310, Lower Hutt 5040, New Zealand

[‡]MacDiarmid Institute for Advanced Materials and Nanotechnology, Victoria University of Wellington, P.O. Box 600, Wellington 6040, New Zealand

[§]School of Chemical and Physical Sciences, Victoria University of Wellington, P.O. Box 600, Wellington 6040, New Zealand

[∥]Stanford Synchrotron Radiation Lightsource, SLAC National Accelerator Laboratory, 2575 Sand Hill Road, Menlo Park, California 94025, United States

Supporting Information

ABSTRACT: The processes of aggregation and subsequent grain growth of highly twinned, surfactant stabilized gold nanoparticles have been followed in real time using synchrotron X-ray diffraction (XRD) and small-angle X-ray scattering (SAXS). This gives insight into the overall coalescence mechanism of metal nanocrystals. First, the capping ligands melt or desorb, which enables the nanocrystals to aggregate and join together. At longer times, grain growth is observed, and the stacking fault densities decrease. The time scale of the grain growth process is significantly longer than that of the particle aggregation. We contrast the behavior we observe to that of other nanoparticles and discuss the implications of our results on device fabrication.

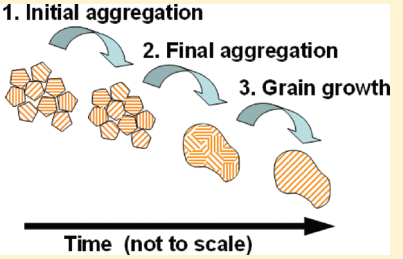

KEYWORDS: nanoparticles, coalescence, grain growth, X-ray diffraction, small-angle X-ray scattering

INTRODUCTION

The coalescence of metallic nanoparticles is one method of bottom-up fabrication of micro- and nanosized electrical devices. Crystal defects such as stacking faults and grain boundaries greatly affect the electrical properties of these coalesced structures. Therefore an understanding of the mechanism of the coalescence in metal nanostructures is needed. Coalescence is key to the application of nanoparticles in electrical devices in terms of both stability and robustness. Once in contact, a pair, or group of nanoparticles will coalesce to reduce their surface energy, as confirmed by in situ observations[1−3] and by molecular dynamics simulations.[4−7] Typically, the nanoparticles will initially form a neck, followed by relaxation to a quasi-spherical shape.[1] Below the melting temperature, surface diffusion is expected to be the dominant mass transport mechanism for the coalescence of nanoparticles,[8] and thus surface processes will control coalescence.

It has been recognized for some time that in nanoscale systems, grain boundaries act as electron scatterers and increase the resistivity of thin films and nanowires.[9−14] Crystallite size in nanograined Au thin films has been shown to have a strong effect on film resistivity, independent of film thickness, and annealing improved the films' electrical conductivity.[9] The presence of grain boundaries has been shown to dominate the scattering of conduction electrons more than surfaces in nanoscale systems.[10−14] This is particularly the case where the size of the grains is comparable to the electron mean free path length (10−100 nm for certain metals[14,15]). Molecular dynamics simulations have also shown that macroscopic sintering theory does not necessarily apply to the coalescence of nanoparticles and that the faceted nature of these particles may be a critical factor in the kinetics of their coalescence.[5] Nonetheless, the electrical resistivity of a nanowire or other such structure is a bulk property (the combined effect of many grains). The effect of grain boundaries, and their removal through annealing processes, is an important aspect to understand the bottom-up fabrication of electrical devices and their subsequent performance.

Clear definitions of the processes discussed in this manuscript are required. We use the term coalescence to refer to the overall particle growth, where the initial stages comprise the aggregation of separate particles (without necessarily adopting the same crystal orientation), followed by subsequent grain growth.

In this article, we report on a real-time in situ observation of the coalescence of gold nanoparticles, which have been synthesized in solution in a Fischer−Porter bottle reaction.[16−18] We demonstrate the aggregation and subsequent grain growth of Au nanoparticles using synchrotron small-angle X-ray scattering (SAXS) and X-ray diffraction (XRD). These complementary methods enable us to follow the initial process of nanoparticles joining together, followed by subsequent grain growth.

Received: February 3, 2011
Revised: May 8, 2011
Published: June 28, 2011

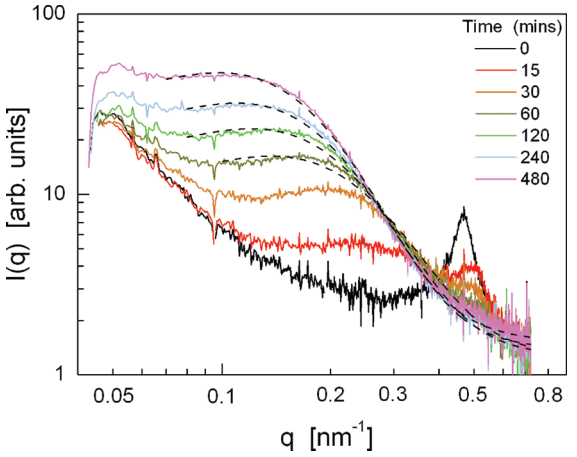

Figure 1. Selected SAXS time series data (colored lines) and fits (dashed lines) for a sample heated at 250 °C.

This enables a more complete description of nanocrystal coalescence and shows that for optimal film formation, care must be taken in the choice of annealing temperature and time.

EXPERIMENTAL SECTION

Au nanoparticles were synthesized via a solution method in a Fischer−Porter bottle as reported previously.[19] The particles are capped with oleylamine as a surfactant and suspended in toluene, and are highly monodisperse with a diameter of 10 nm.

Synchrotron experiments were conducted at the Stanford Synchrotron Radiation Lightsource. The samples were prepared by placing 5 drops of the colloidal Au nanoparticle suspension (22 g/L) on a substrate (mica for SAXS and silicon wafer for XRD) and allowing the solvent to evaporate in between each drop. This results in an average coverage of approximately 200 layers of particles. SAXS was performed at beamline 1−4 with an X-ray wavelength of 1.488 Å and a sample−detector distance of 2 m. The samples were measured in transmission using a CCD detector, with collection times of 1−2 min at the start of an experiment, lengthening to 5−10 min at the later stages. A custom built furnace was used to heat each sample to a temperature between 150 and 350 °C (maximum heating rate ∼40 °C min^{-1}), which was then held constant while data were collected. SAXS data were fitted using SAXSFit.[20,21] XRD experiments were conducted at beamline 7−2 with an X-ray wavelength of 0.775 Å and a Vortex detector with 1 mrad Soller slits for collimation of the diffracted beam (i.e., instrument resolution ∼0.06° in 2θ). The samples were heated to 250 or 350 °C using an Anton-Parr DS-950 heating stage (maximum heating rate ∼40 °C min^{-1}). The measurements were conducted using a grazing incidence (α = 0.2°) asymmetric Bragg geometry to increase the scattering volume. Typical scan times were 8−9 min. Transmission electron microscopy (TEM) was performed using a JEOL 2011 microscope with a LaB_6 filament operated at 200 kV. Samples were prepared by putting one drop of the toluene nanoparticle suspension onto a supported-carbon TEM grid and allowing the solvent to evaporate under ambient conditions.

RESULTS AND DISCUSSION

Figure 1 shows SAXS data for a sample heated at 250 °C for 8 h. The initial SAXS pattern of the as-deposited nanoparticulate film exhibits a sharp correlation peak at q = 0.45 nm^{-1}. This corresponds to a close packed arrangement of the highly monodisperse Au particles, shown by TEM in Figure 2. The average

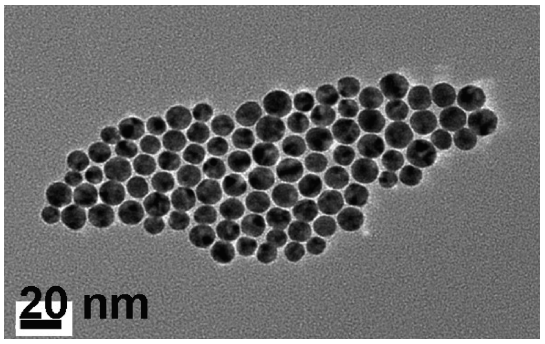

Figure 2. TEM image of the as-prepared Au nanoparticles, showing a close-packed arrangement.

particle spacing can be estimated from the peak position ($2\pi/q_{peak}$) to be 14 nm. This is slightly larger than the size of the gold nanoparticles shown in the TEM image (Figure 2), which is consistent with the presence of a surfactant shell around the particles (10−12 nm in diameter).

As the film is heated, the initial peak moves to a slightly higher q of 0.5 nm^{-1} and broadens. Additionally a there is a rapid development of a broad feature at lower q values. This corresponds with aggregation of the particles.

The initial shift of the peak from 0.45 nm^{-1} to 0.5 nm^{-1} corresponds to a decrease in the interparticle distance from 14 to 12 nm (the particle size without the surfactant). Melting or desorption of the oleylamine exposes the surfaces of the particles, and since they are closely packed, they quickly begin to interact and aggregate. This process does not happen below 150 °C, as evidenced by monitoring one sample for over 10 h at 150 °C and observing no change in the shape, intensity, or position of the correlation peak. Indeed, thermogravimetric analysis (Figure S1, Supporting Information) shows that the oleylamine surfactant is removed at temperatures above 165 °C.

The low Q, broader feature in SAXS was fitted using a local monodisperse approximation hard sphere model,[20] implemented in the SAXSFit fitting program,[21,22] to obtain the mean aggregate size as a function of time. This is shown in Figure 4a. The initial increase in the aggregate size is rapid but slows over time as the surface diffusion (driven by a reduction in nanoparticle curvature) slows down. Satisfactory fits to the SAXS data could only be obtained for later times, after the initial correlation peak had disappeared. Once the local nanoparticle ordering is broken, the local monodisperse approximation is valid for the coalescing particle system.

SAXS has previously been used to study particle size changes in Pt and Pt−Cu catalytic nanoparticles under electrochemical conditions[23,24] with an average size resolution of less than 0.1 nm in the average particle size. Thus, SAXS is a robust technique for determining the average size of a nanoparticle ensemble.

Korgel et al.[25] have also used SAXS to study the ordering of Ag nanoparticle arrays as a function of temperature. In the initial stages, distinct peaks are observed in the SAXS pattern corresponding to face-centered cubic packing of the particles. As the array is heated, changes are observed in the position and intensity of these peaks, from which a mechanism for the melting (disordering) of the array and subsequent coalescence of the particles was inferred (although the development of the overall aggregate size was not reported). Since we only observe one correlation peak in our SAXS data (corresponding to the nearest

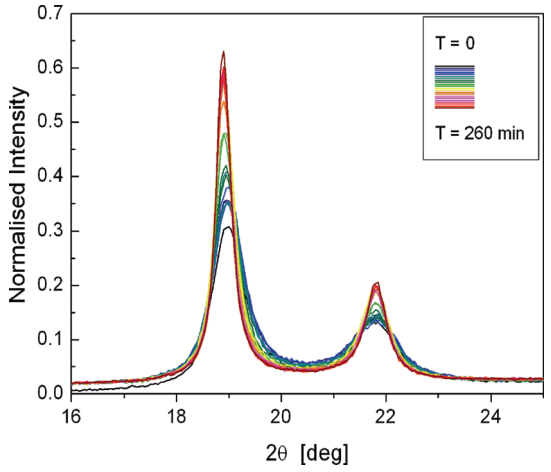

Figure 3. XRD time series for a sample heated at 250 °C.

particle−particle distance), our particles do not form arrays as regular as those of Korgel et al.

As the gold nanoparticles are heated, the following processes are expected to occur. First, stacking faults will anneal out of individual nanoparticles; second (and possibly concurrently), the nanoparticles will aggregate, and these aggregates will eventually become single-grained particles. To follow these processes, XRD patterns of the gold nanoparticles were recorded during heating.

The XRD data shown in Figure 3 represent a time series collected while the sample was held at a temperature of 250 °C for approximately 4 h. The Au (111) and (200) peaks were monitored and were seen to start off as small broad peaks that became sharper over time. Diffraction peaks are broadened by finite crystallite size, lattice deformations (inhomogeneous strain), and planar lattice defects. The most significant of these in nanoparticles are usually crystallite size and planar defects. Stacking faults are common planar defects in face-centered cubic (fcc) metals and occur where the *ABCABC* packing of the atomic layers is interrupted. Here *A*, *B*, and *C* are (111) atomic planes. Deformation faults occur where one of the packing layers is missing (e.g., *ABCBCABC*). Twin faults occur where there is a reversal in the packing sequence (e.g., *ABCBA*). (Note that these are referring to the arrangement of atoms within the individual particles/grains, not the arrangement of the particles.) The coherence length (the size of the coherently diffracting region) is therefore limited by not only the crystallite size, but also the number of crystal planes between faults (1/fault density). The two effects can be deconvoluted by comparing multiple peaks because deformation faults also cause the peak positions to be shifted slightly depending on their *hkl*-index, and twin faults cause certain peaks to be broadened more than others. The contribution to the peak width from the fault densities can thus be deconvoluted and the crystallite size obtained.

The effective coherence length, D_{eff}, is calculated using the Scherrer equation[26]

$$D_{eff} = \frac{c\lambda}{fwhm(2\theta)cos\ \theta} \quad (1)$$

where c is a shape correction factor, normally 0.94 for cubic crystals, λ is the X-ray wavelength, fwhm(2θ) is the full-width-at-half-maximum in radians, and 2θ is the scattering angle. The (111) and (200) peaks were observed to move apart by ~0.1° (2θ) over the course of annealing. The deformation fault density α is calculated from Warren[26] as follows:

$$\Delta(2\theta_{200} - 2\theta_{111})^\circ = \frac{-90\sqrt{3}\alpha}{\pi^2}\left(\frac{tan\ \theta_{200}}{2} + \frac{tan\ \theta_{111}}{4}\right) \quad (2)$$

where $\Delta(2\theta_{200} - 2\theta_{111})^\circ$ is the difference in peak separation compared to that expected for no faulting, and $2\theta_{hkl}$ is the scattering angle for the (*hkl*) peak.

The deconvolution of D_{eff} was obtained from

$$\frac{1}{D_{eff}^2} = \frac{1}{D^2} + \frac{(1.5\alpha + \beta)^2}{a^2} C_{hkl}^2 \quad (3)$$

where a is the cubic lattice parameter, D is the crystallite size, and β is the twin fault density. C_{hkl} is a numeric factor determined from the reflection index (*hkl*), and has values $(3^{(1/2)})/4$ for the (111) reflection and 1 for the (200) reflection. By considering the (111) and (200) reflections together, and using α obtained from eq 2, D and β can be obtained.

For systems following a Poisson size distribution, it is appropriate to use a simple linear deconvolution method to extract D and β, as given by Warren.[26] However, for monodisperse nanoscale systems such as that considered here, the linear method yields erroneously high values for D.

Instead of considering a sum of linear components, we considered summing the squares of each component; this is

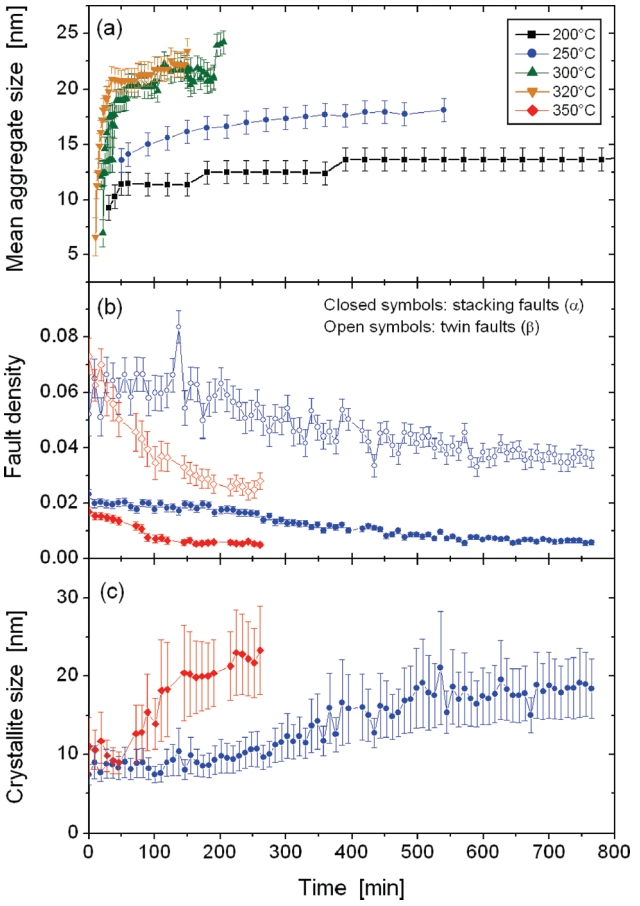

Figure 4. Comparison of results obtained from the SAXS and XRD experiments: (a) mean aggregate size, (b) deformation and twin fault densities, and (c) crystallite size.

appropriate for systems with monodisperse crystallite size distributions. Thus, the two equations being deconvoluted become

$$\frac{1}{D_{eff(111)}^{\ 2}} = \frac{1}{D^2} + \frac{3}{16}\frac{(1.5\alpha+\beta)^2}{a^2}\frac{1}{D_{eff(200)}^{\ 2}}$$

$$= \frac{1}{D^2} + \frac{(1.5\alpha+\beta)^2}{a^2}$$

This yielded satisfactory values for both D and β.

The deformation fault density α, twin fault density β, and the crystallite size D are plotted against time in Figure 4b and c, respectively.

The deformation fault density α has an initial value of approximately 0.02 and decreases over time to a value of approximately 0.005. The twin fault density β has an initial value of approximately 0.065. Both α and β start to drop at about the same time that the crystallite size starts to increase (see Figure 4).

The initial values of α and β are consistent with literature values for the stacking fault density expected for 10 nm multiply twinned particles. Icosahedra and decahedra, both common morphologies for small nanoparticles, are formed by arranging triangular and/or square pyramids. Stacking faults occur at boundaries between two triangular or two square pyramids, whereas no fault occurs at the boundary between a triangular and square pyramid.[27] An icosahedron consists of 20 triangular pyramids, with 12 vertices and 30 boundaries. A decahedron consists of 10 triangular pyramids, with 7 vertices and 15 triangular−triangular boundaries resulting in stacking faults. Therefore, the icosahedron has twice the stacking fault density or probability of a decahedron of the same size. For a 10 nm icosahedron, the deformation fault density is reported as being 0.05.[28] Experiments on fcc Pd (particle diameter ~4 nm) yield values for β between 0.12 and 0.15 (α was assumed to be zero).[29] Experiments on annealed Au samples (5 nm diameter particles) give a value for $(1.5\alpha + \beta)$ of 0.036,[30] which is comparable with our results. Therefore, the experimental values obtained are consistent with the initial particles being heavily twinned, perhaps decahedral, with these deformations mostly annealed out over time. TEM shows evidence for at least some of the particles being decahedral,[19] but one must remember that TEM is a localized observation, while XRD measures an ensemble average.

As can be seen by the different time dependencies of mean aggregate size, fault densities and crystallite size (Figure 4), there are different processes occurring with different rates. For example, the two mean aggregate size curves at 300 and 320 °C approach a plateau after approximately 150 and 50 min, respectively. However, at a higher temperature (350 °C), the plots obtained from the XRD measurements show that changes in the fault densities and the crystallite size continue to evolve at longer times, up to 200 min. Therefore, at the same temperature, the grains continue to grow long after the aggregation of the particles is complete.

From the combined XRD, TEM, and SAXS data, it is possible to build up a picture of the processes occurring in the gold nanoparticles as they are heated. The mechanism of aggregation and subsequent grain growth is shown schematically in Figure 5. In the initial stage, the particles form a close packed arrangement, with the oleylamine surfactant acting as a spacer keeping the particles apart.

Step 1: as the temperature rises above 165 °C, the oleylamine capping molecules melt or desorb, and the particles begin to aggregate as shown from the change in the SAXS data.

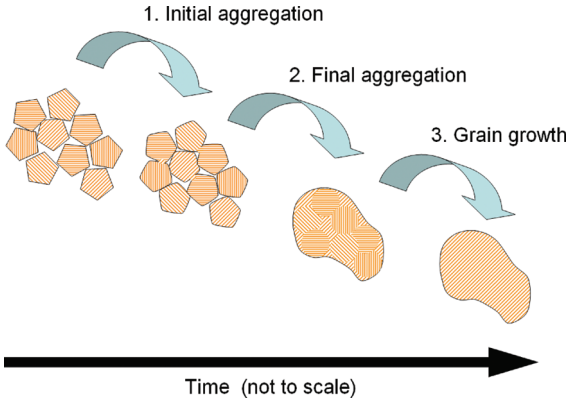

Figure 5. Schematic diagram showing the mechanisms of coalescence.

Step 2 (between 15 and 100 min at 250 °C): the nanoparticles begin to join together as shown by the change of the peak position in the SAXS data. This likely begins with the formation of necks between the particles and is driven by surface atom diffusion to minimize the surface area.[19,31] As aggregate growth stops, the aggregate still consists of multiple grains. After this time, the SAXS data change very little since the SAXS arises from the total aggregate size. However, both the deformation and twin fault densities start to decrease.

Step 3 (between 200 and 500 min at 250 °C): grain growth continues, as observed in XRD from the changes in the Au (111) and (200) peak widths and relative positions. The deformation and twin fault densities continue to decrease.

The mechanism of overall particle aggregation (steps 1 and 2 above) agrees with Moon et al.[32] Our results yield additional insight into the grain growth behavior in addition to the particle growth behavior, highlighting the fact that the grain growth stage takes significantly longer than the particle aggregation stage. Since it is the grain boundaries that affect electrical conduction, this difference in annealing times required is important to take into consideration when assembling nanoscale devices through thermal annealing.

These results have implications for determining appropriate temperature−time annealing profiles in the fabrication of nanoscale devices from nanoparticles, in cases where a low-temperature ($\ll T_{m,bulk}$) thermal annealing process is used to induce coalescence.[1−3,33] The results are also significant for indicating the range of the thermal stability of any devices made from nanocrystals such as solar cells[34,35] and magnetic storage media,[36] where the coalescence of particles is undesirable. Devices relying on the properties of discrete nanoparticles need to be kept below the temperature at which step 1 occurs. Some devices need to operate with nanoparticles touching; in this case, they need to be taken to step 2. However if step 3 starts to occur, then the nanograin properties (i.e., quantum confinement) will be lost. The exact temperatures will depend strongly on the metal system, the surfactant system (if any), the substrate, and the particle size. For example, 9−13 nm Co particles start to coalesce between 100 and 200 °C, as evidenced by a drop in film resistivity;[37] Fe particles 19 nm in size start to coalesce above 277 °C (550 K);[38] nanocrystalline Ni with 20 nm crystallites exhibits an increase in crystallite size above 327 °C (600 K).[39] It is also possible to induce the coalescence of small particles by removing the surfactant through evaporation of the solvent, rather than thermal desorption of the surfactant. This has been

dx.doi.org/10.1021/cm200354d |Chem. Mater. 2011, 23, 3312–3317

reported at room temperature for Ag particles 11 nm[40] and 16 nm[41] in size (with both studies showing dramatic drops in film resistivity consistent with coalescence) and at solution temperatures of 50 °C for Au particles 5−8 nm in size.[32]

Previous work on thermally induced coalescence of Au nanoparticles generally relies on electron microscopy to obtain information about particle size distributions.[42,43] Turba et al.[42] studied Au nanoparticles deposited on GaN nanowires using SEM and obtained an Arrhenius relationship for the nanoparticle growth rate as a function of temperature. Meli and Green[43] studied the thermal annealing behavior of 5 nm Au particles in polymer films using TEM and inferred that particle growth at 150 °C progressed initially by Ostwald ripening and aggregation (which they term coalescence), followed by aggregation. We do not see any evidence for Ostwald ripening. In Ostwald ripening the adatoms would be expected to adopt the same orientation as the particle to which they attach, thus increasing the crystallite size. However, in this work the crystallite size is constant during steps 1−2 and only increases once the particles have mostly coalesced. This may be due to the environment the particles are in: our surfactant-coated particles are likely to be more mobile than particles embedded in a polymer film, and therefore, aggregation is the preferred mechanism in our case.

Coalescence in Au nanoparticles as a result of heating by the electron beam has also been reported.[44,45] Chen et al.[44] reported a TEM study of Au particles of varying sizes (2.8−4.8 nm diameter) and concluded that the coalescence mechanism was dominated by surface diffusion of atoms as opposed to Ostwald ripening. They also noted differences based on the surfactant system used. Ristau et al.[45] reported a TEM study of particles that were subjected to both thermal heating and electron beam heating to induce coalescence. They concluded that while the two processes were similar, the heating rate used in the thermal study had a significant effect on the sintering behavior (coarsening vs densification). One conclusion that can be drawn from these studies is that extreme care is needed when performing in situ TEM, or indeed, even when capturing images, since only low electron doses can result in coalescence.

CONCLUSIONS

In summary, the processes of aggregation of surfactant stabilized, highly twinned gold nanoparticles and the subsequent grain growth have been followed in real time using synchrotron XRD and SAXS. Through the use of these complementary techniques, our work has elucidated a more complete picture of the coalescence mechanism of metal nanocrystals by following both the particle and crystallite size dynamics. SAXS data show that initial heating of the nanocrystals causes them to aggregate and join together as capping ligands melt or desorb. In later stages at higher temperature and longer times, crystal grain growth and a reduction in the fault densities are observed by XRD. These results are of critical importance for the use of thermally coalesced metal nanocrystals in micro- and nanosized electrical devices: the time scales required for the crystallite sizes to nearly equilibrate are considerably longer than those required for the initial aggregation of the particles. This suggests that when annealing these nanoparticles, there will be a conductivity onset after the initial aggregation (the beginning of step 1 in Figure 5) but that the conductivity will continue to increase until grain growth slows (Figure 5, step 2).

ASSOCIATED CONTENT

Supporting Information. Thermogravimetric analysis of the as-prepared Au nanoparticles (PDF). This material is available free of charge via the Internet at http://pubs.acs.org.

AUTHOR INFORMATION

Corresponding Author
*E-mail: b.ingham@irl.cri.nz.

ACKNOWLEDGMENT

Portions of this research were carried out at the Stanford Synchrotron Radiation Lightsource, a national user facility operated by Stanford University on behalf of the U.S. Department of Energy, Office of Basic Energy Sciences. Funding was provided in part by the New Zealand Foundation for Research, Science and Technology under contract CO8X0409. We thank John Pople and Valery Borzenets for the synchrotron beamline support.

REFERENCES

(1) Bonevich, J. E.; Marks, L. D. *J. Mater. Res.* **1992**, *7*, 1489–1500.
(2) Palasantzas, G.; Vystavel, T.; Koch, S. A. *J. Appl. Phys.* **2006**, *99*, 024307.
(3) Dai, Z. R.; Sun, S.; Wang, Z. L. *Nano Lett.* **2001**, *1*, 443–447.
(4) Zhu, H.; Averback, R. S. *Philos. Mag. Lett.* **1996**, *73*, 27–33.
(5) Lewis, L. J.; Jensen, P.; Barrat, J. L. *Phys. Rev. B* **1997**, *56*, 2248–2257.
(6) Zachariah, M. R.; Carrier, M. J. *J. Aerosol Sci.* **1999**, *30*, 1139–1151.
(7) Hendy, S.; Brown, S. A.; Hyslop, M. *Phys. Rev. B* **2003**, *68*, 241403.
(8) Mullins, W. *J. Appl. Phys.* **1957**, *28*, 333–339.
(9) de Vries, J. W. C. *J. Phys. F: Met. Phys.* **1987**, *17*, 1945–1952.
(10) Mayadas, A. F.; Shatzkes, M. *Phys. Rev. B* **1970**, *1*, 1382–1389.
(11) Steinhögl, W.; Schindler, G.; Steinlesberger, G.; Traving, M.; Engelhardt, M. *J. Appl. Phys.* **2005**, *97*, 023706.
(12) Wu, W.; Brongersma, S. H.; Van Hove, M.; Maex, K. *Appl. Phys. Lett.* **2004**, *84*, 2838–2840.
(13) Sun, T.; Yao, B.; Warren, A. P.; Barmak, K.; Toney, M. F.; Peale, R. E.; Coffey, K. R. *Phys. Rev. B* **2009**, *79*, 041402(R).
(14) Rossnagel, S. M.; Kuan, T. S. *J. Vac. Sci. Technol. B* **2004**, *22*, 240–247.
(15) Ashcroft, N. W.; Mermin, N. D. *Solid State Physics*; Brooks/Cole: New York, 1976; p 52.
(16) Cheong, S.; Watt, J.; Ingham, B.; Toney, M. F.; Tilley, R. D. *J. Am. Chem. Soc.* **2009**, *131*, 14590–14595.
(17) Watt, J.; Young, N.; Haigh, S.; Kirkland, A.; Tilley, R. D. *Adv. Mater.* **2009**, *21*, 2288–2293.
(18) Watt, J.; Cheong, S.; Toney, M. F.; Ingham, B.; Cookson, J.; Bishop, P. T.; Tilley, R. D. *ACS Nano* **2010**, *4*, 396–402.
(19) Lim, T. H.; McCarthy, D.; Hendy, S. C.; Stevens, K. J.; Brown, S. A.; Tilley, R. D. *ACS Nano* **2009**, *3*, 3809–3813.
(20) Pedersen, J. S. *J. Appl. Crystallogr.* **1994**, *27*, 595–608.
(21) Ingham, B.; Li, H.; Allen, E. L.; Toney, M. F. *SAXSFit: A Program for Fitting Small-Angle X-ray and Neutron Scattering Data*; arXiv:0901.4782.
(22) http://www.irl.cri.nz/SAXSfiles.
(23) Smith, M. C.; Gilbert, J. A.; Mawdsley, J. R.; Seifert, S.; Myers, D. J. *J. Am. Chem. Soc.* **2008**, *130*, 8112–8113.
(24) Yu, C.; Koh, S.; Leisch, J. E.; Toney, M. F.; Strasser, P. *Faraday Discuss.* **2008**, *140*, 283–296.
(25) Korgel, B. A.; Zaccheroni, N.; Fitzmaurice, D. *J. Am. Chem. Soc.* **1999**, *121*, 3533–3534.

(26) Warren, B. E. *X-ray Diffraction*; Dover Publications Inc.: New York, 1969; p 288−294.
(27) Soler, J. M.; Garzon, I. L.; Joannopoulos, J. D. *Solid State Commun.* **2001**, *117*, 621–625.
(28) Kovalenko, S. I.; Solnyshkin, D. D.; Verkhovtseva, E. T.; Eremenko, V. V. *Chem. Phys. Lett.* **1996**, *250*, 309–312.
(29) Martorana, A.; Deganello, G.; Duca, D.; Benedetti, A.; Fagherazzi, G. *J. Appl. Crystallogr.* **1992**, *25*, 31–38.
(30) Vogel, W.; Bradley, J.; Vollmer, O.; Abraham, I. *J. Phys. Chem. B* **1998**, *102*, 10853–10859.
(31) Arcidiacono, S.; Bieri, N. R.; Poulikakos, D.; Grigoropoulos, C. P. *Int. J. Multiphase Flow* **2004**, *30*, 979–994.
(32) Moon, S. Y.; Tanaka, S.-I.; Sekino, T. *Nanoscale Res. Lett.* **2010**, *5*, 813–817.
(33) Volkman, S. K.; Pei, Y.; Redinger, D.; Yin, S.; Subramanian, V. *Mater. Res. Soc. Symp. Proc.* **2004**, *814*, I7.8.1.
(34) Huynh, W. U.; Dittmer, J. J.; Alivisatos, A. P. *Science* **2002**, *295*, 2425–2427.
(35) Panthani, M. G.; Akhavan, V.; Goodfellow, B.; Schmidtke, J. P.; Dunn, L.; Dodabalapur, A.; Barbara, P. F.; Korgel, B. A. *J. Am. Chem. Soc.* **2008**, *130*, 16770–16777.
(36) Sun, S.; Anders, S.; Thomson, T.; Baglin, J. E. E.; Toney, M. F.; Hamann, H. F.; Murray, C. B.; Terris, B. D. *J. Phys. Chem. B* **2003**, *107*, 5419–5425.
(37) Peng, D. L.; Konno, T. J.; Wakoh, K.; Hihara, T.; Sumiyama, K. *Eur. Phys. J. D* **2001**, *16*, 329–332.
(38) Natter, H.; Schmelzer, M.; Löffler, M. S.; Krill, C. E.; Fitch, A.; Hempelmann, R. *J. Phys. Chem. B* **2000**, *104*, 2467–2476.
(39) Eastman, J. A.; Beno, M. A.; Knapp, G. S.; Thompson, L. J. *Nanostruct. Mater.* **1995**, *6*, 543–546.
(40) Magdassi, S.; Grouchko, M.; Berezin, O.; Kamyshny, A. *ACS Nano* **2010**, *4*, 1943–1948.
(41) Wakuda, D.; Kim, K. S.; Suganuma, K. *Scripta Mater.* **2008**, *59*, 649–652.
(42) Turba, T.; Norton, M. G.; Niraula, I.; McIlroy, D. N. *J. Nanopart. Res.* **2009**, *11*, 2137–2143.
(43) Meli, L; Green, P. F. *ACS Nano* **2008**, *2*, 1305–1312.
(44) Chen, Y.; Palmer, R. E.; Wilcoxon, J. P. *Langmuir* **2006**, *22*, 2851–2855.
(45) Ristau, R.; Tiruvalam, R.; Clasen, P. L.; Gorskowski, E. P.; Harmer, M. P.; Kiely, C. J. *Gold Bull.* **2009**, *42*, 133–143.